Original Article

Bulletin of Pure and Applied Sciences.
Vol.37 C (Chemistry), No.1, 2018: P.99-106
Print version ISSN 0970 4620
Online version ISSN 2320 320X
DOI 10.5958/2320-320X.2018.00013.4

Synthesis, structural characterization and uv analysis of praseodymium zirconate oxides

S. Srijith[1*], V. T. Kavitha[2], L.R. Asitha[1]

Author Affiliations
[1]Research and Post graduate Department of Physics, SN College, Kollam, Kerala, India.
[2]Research and Post graduate Department of Physics, Mahatma Gandhi College, Thiruvananthapuram, Kerala, India.

Corresponding Author
***S. Srijith,** Research and Post graduate Department of Physics, SN College, Kollam, Kerala, India.

E-mail: srijithkeanu@gmail.com

Received on 13th January 2018
Accepted on 24th January 2018

Abstract

Nanoceramics can be utilized for various applications like electronic, ionic, thermal, optical and catalytic. In particular, the combination of a relatively large portion of interfacial or grain boundary atoms along with the interactions of photons, electrons, or dislocations can lead to unusual mechanical and electrical behavior. In this work, we synthesize $Pr_2Zr_2O_7$ oxides through solution combustion synthesis and study the band gap of the material. The effect of strain on the broadening of X ray peaks were also analysed using Hall Williamson analysis.

Keywords: Nanoceramics, Oxides, $Pr_2Zr_2O_7$, Crystallite size

1. INTRODUCTION

Nano–ceramics have received a considerable attention during the last two decades due to their capability to demonstrate improved or unique characteristics as compared to conventional bulk ceramic materials. Nano–ceramics can be utilized for various applications like electronic, ionic, thermal, optical and catalytic. In particular, the combination of a relatively large portion of interfacial or grain boundary atoms along with the interactions of photons, electrons, or dislocations can lead to unusual mechanical and electrical behaviour.

Among the ternary metallic oxides, compounds of the general formula, $A_2B_2O_7$ (A and B are metals), represent a family of phases isostructural to the mineral pyrochlore, (NaCa) $(NbTa)O_6F/(OH)$ [1]. Thespace group of the ideal pyrochlore structure is Fd3m and there are eight molecules per unit cell (Z=8). In $A_2B_2O_7$ pyrochlores, A is usually a trivalent rare earth ion, but can also be a mono, divalent cation and B may be 3d, 4d or 5d transition element having an appropriate oxidation state required for charge balance to give rise to the composition $A_2B_2O_7$ [2]. Pyrochlore unit cell contains eight A_2 B_2 $O(1)_6$ O(2) formula units, and for better and easy understanding one–eighth of the

pyrochlore unit cell is shown in figure 1. With the choice of B atom as origin, the cation sublattice is an alternate arrangement of A–site (16*d*) and B–site (16*c*) cations along the 110 direction in an fcc lattice. The anion sublattice is comprised of three different oxygen sites, two of which are occupied (8*b*) and (48*f*), and the third site (8*a*) is vacant. Hence, the anion vacancies are ordered. The A–site cations are eight coordinated and are located within scalenohedra (distorted cubes). The B–site cations are six–coordinated and are located within trigonal antiprisms. All anion sites are tetrahedrally coordinated: the 8*a* site is surrounded by four B cations, and the 8*b* site by four A cations. The 48*f* oxygen is surrounded by two A and two B cations that are slightly displaced from the center of the tetrahedral site towards the unoccupied 8*a* site. The magnitude of the displacement is represented by the positional parameter, *x*, of oxygen at the 48*f* site, which is 0.375 for the ideal fluoritestructure. The pyrochlore crystal structure also tolerates vacancies at the A and O sites to a certain extent with the result that cation and anion migration within the solid is feasible. Recently, it has been shown by our group that anion rich pyrochlores like $Ce_2Zr_2O_8$ are also possible [3]. The pyrochlore structure is closely related to the fluorite structure AX_2, except that there are two cation sites and one–eighth of the anions are absent as shown in the Figure 1 for the ordered pyrochlore, $A_2B_2O_7$, the phase stability of the superstructure is basically determined by the A and B site cation radius ratio.

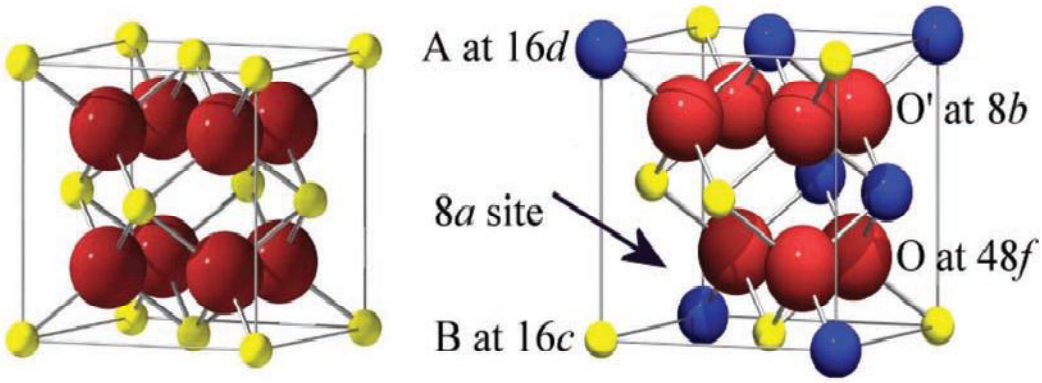

Fig. 1: (a): Unit cell of fluorite (Fmm), yellow atoms represent A^{4+} cations and the red O^{2-} and (b): Unit cell of pyrochlore (Fd3m), Blue spheres represent A^{3+} cations, yellow $B^{4+}$and red O^{2-}

It is worth noting here that compounds with similar cationic radii are more likely to form as disordered fluorites than ordered pyrochlores, for instance,$Er_2Zr_2O_7$ having r_A/r_B ~1.39 crystallizes as a disordered fluorite structure whereas $Er_2Ti_2O_7$ with r_A/r_B ~1.66 crystallizes as a ordered pyrochlore structure. Since more number of (3+, 4+) ions are possible, therefore, large number of pyrochlores having (3+, 4+) cations are reported in literature compared to pyrochlores having (2+, 5+) cations. Recently, (1+, 6+) pyrochlores like KOs_2O_6 are reported in the literature [4,5,6]. In general, pyrochlores exhibit a wide variety of interesting physical properties because a diverse range of constituent ions can be chosen to obtain the desired properties. The pyrochlore structure exhibits a greater degree of complexity than the fluorite structure. The cubic pyrochlore structure is similar to the cubic fluorite structure but with a large number of the oxygen atoms displaced (and one in eight missing). In this work, we synthesize $Pr_2Zr_2O_7$ oxides through solution combustion synthesis and study the band gap of the material.

2. EXPERIMENTAL

Among the available, solution chemistry routes, the solution combustion techniques are capable of producing the nanocrystalline powders of oxide ceramics at a lower calcination temperature in a surprisingly short time [7, 8]. Generally the powder obtained by this technique has compositional homogeneity, the highest degree of phase purity coupled with the improved powder characteristics like narrow particle size distribution, higher surface area and better sinterability;but those depend heavily on the adopted processing parameters. All the oxide materials were prepared by the combustion of aqueous solutions containing stoichiometric amounts of corresponding metal nitrates

and citric acid redox mixtures in a Pyrex dish. Stoichiometry of the redox mixture for the combustion is calculated based on the total oxidizing and reducing valencies of the oxidizer (O) and of the fuel (F), which serve as numerical coefficients so that the equivalence ratio, f_e (O/F), becomes unity and the heat released is at a maximum [9,10]. According to the principles used in propellant chemistry, the oxidizing and reducing valencies of various elements are considered as follows: C = 4, H = 1, O = –2, N = 0,M = 2, 3, 4, etc. Thus, the oxidizing valency of a divalent metal nitrate, M $(NO_3)_2$ becomes –10; $M(NO_3)_3$ = –15; $M(NO_3)_4$= –20; and the reducing valency of HMT ($C_6H_8O_7$) becomes +18. Therefore, the molar ratio of the divalent metal nitrate to fuel (citric acid is) is 15/36, i.e., 1:0.4166. The exothermicity of combustion reactions as well as combustion time can be increased by the presence of redox compounds, such as NH_4NO_3/NH_3ClO_4. This will facilitate the formation of the pure crystalline phase and doping.

A mixture of high purity Pr_2O_3 (2.0205gm), ZrO $(NO_3)_2$ $2H_2O$ (2.9794gm) and citric acid (5.2585gm) are taken in a beaker. After mixing the metal nitrate solutions in beaker, 30 ml nitric acid is added and stirred continuously for 30 minutes. The fuel used for the synthesis is citric acid. In order to attain a pH of 7, liquor ammonia is added drop by drop and the solution is heated at 100 ºC to remove as much of water content. After evaporation of the water content, the slurry was then introduced into a muffle furnace preheated to 400°C. The mixture frothed and ignited to combust with a flame, giving a voluminous and foamy $Pr_2Zr_2O_7$.The structure and phase purity of the powder were examined by XRD using Regaku, DMax C, Japan X– ray diffractometer with Nickel filtered Cu K_α radiation. The UV–visible spectra of samples were recorded by dispersing the sample in ethanol medium using an ultrasonic bath. The absorption spectra were recorded at room temperature using SHIMADZU–2550 UV–Visible Spectrophotometer in the range from 200–800 nm.

3. RESULTS AND DISCUSSIONS

3.1 XRD Analysis

The XRD pattern of the as prepared powder sample obtained by the present combustion synthesis is shown in Figure 2.

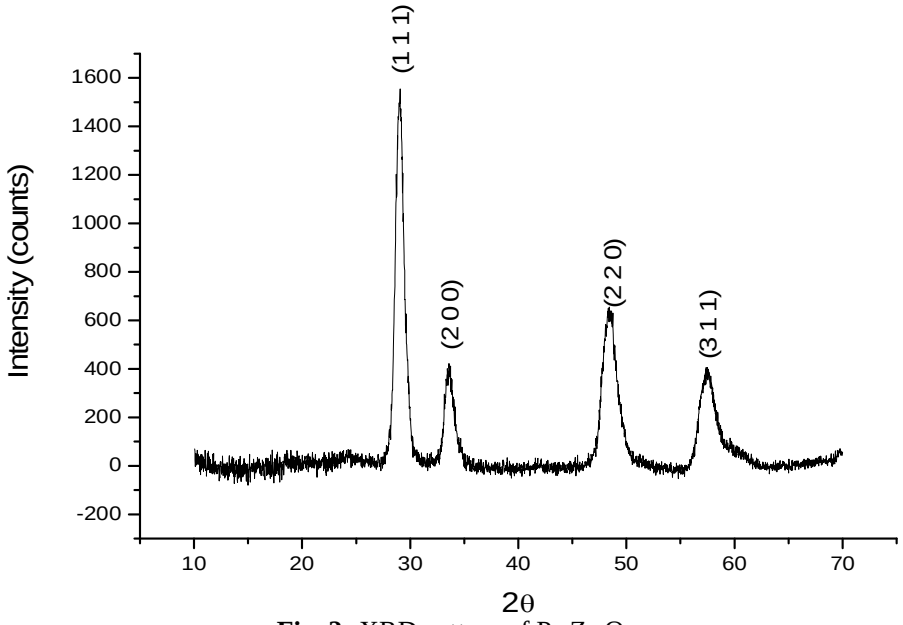

Fig. 2: XRD pattern of $Pr_2Zr_2O_7$

The powder XRD patterns of the sample confirm that the sample is crystalline in nature. Also, the diffraction peak is slightly broadened indicating small crystallite size. High intensity peaks with even–numbered miller indices, representing average fluorite–type unit cells. The superstructure peaks

at 2θ *at*≈14˚, 38˚, 46˚, etc. are very weak in intensity [11, 12]. Progressive structural transformation into defect pyrochlore structure can also lead to a decrease in intensity of the superstructure peaks. Hence it is very difficult to directly determine from the XRD pattern whether the average structure of the compounds is defect pyrochlore or defect fluorite. From the absence of the superstructure peaks, it can be concluded that the structure is defect fluorite [13,14,15]. All the reflections in the Xrd pattern shows that $Pr_2Zr_2O_7$ has cubic lattice, with lattice parameter a = 10.43 Å. Another important observation is that some of the Bragg peaks show asymmetric broadening in contrast to symmetric broadening expected due to strain.

3.2. Determination of Average Crystallite Size Using Scherrer equation

A perfect crystal would extend in all directions to infinity, so we can say that no crystal is perfect due to its finite size. This deviation from perfect crystalline leads to a broadening of the diffraction peaks. However, above a certain size (100–500 nm) this type of broadening is negligible. Crystallite size is a measure of the size of a coherently diffracting domain. Due to the presence of polycrystalline aggregates, crystallite size is not generally the same thing as particle size. In this section the crystallite sizes of sample is determined from X–ray diffraction line broadening using Scherrer equation [16]. Scherrer equation is the simplest method of determining the average crystallite size of a nanocrystalline sample from X–ray diffraction line broadening. Scherrer equation is,

$$t = K\lambda / (\beta_{hkl})_{measured} \times \mathrm{Cos}\theta_{hkl}$$

Here, t is the average crystallite size normal to the reflecting planes, K is the shape factor which lies between 0.95 and 1.15 depending upon the shape of the grains (K=1 for spherical crystallites), λ is the wavelength of X–rays used and $(\beta_{hkl})_{measured}$ is the measured FWHM of the diffraction line in radians and θ_{hkl} is the Bragg angle corresponding to the diffraction line arising from reflections from the planes designated by the Miller indices (h k l). In order to estimate the FWHM the following procedure was adopted. A Pseudo–Voigt 1 function which assumes the peak shape is symmetrical was used to fit the peak profiles. Pseudo–Voigt 1 is one of the most convenient functions used for the profile fitting of X–ray diffraction peaks and it is represented by the expression,

$$y = y_0 + A\left[\frac{2\omega}{\pi\left(x - x_c\right)^2 + \omega^2} + \frac{(1-\mu)\sqrt{4\ln 2}\left(e^{-\frac{4\ln 2(x-x_c)^2}{\omega}}\right)}{\sqrt{\pi}\omega}\right]$$

where, y is the dependent variable (Intensity in the present case), X is the dependent variable (2θ in the present case), ie, X_c is the peak centre, A is the measure of maximum intensity and W is the Full Width at Half Maximum and μ is the profile shape factor. The curve fitting was done using Microcal Origin Version 9. The best fit was chosen taking into account the minimum error as well as the realistic values for individual variables. From Table 1, it can be noted that the average crystallite size of the sample ~18 nm.

Table 1: Scherrer size of crystallites

2θ (°)	θ (°)	FWHM (°)	Crystallite size t, (nm)	
29.02	14.51	0.7957	11.6	9.4nm
33.64	16.82	0.8271	11.3	
48.34	24.17	1.2402	7.9	
57.41	28.71	1.4843	6.9	

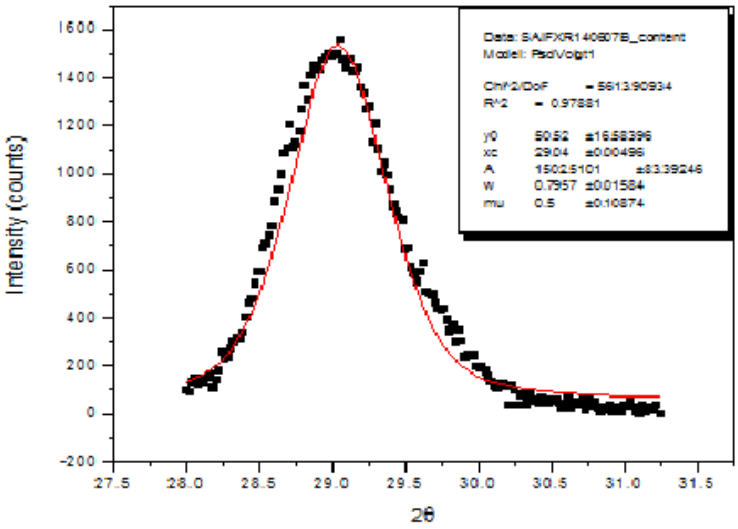

Fig. 3: Peak fitting using pseudo Voigh 1 function

3.3. Hall–Williamson Method to Separate Crystallite Size and Strain Broadening

Hall–Williamson analysis of the nanocrystalline samples is carried out assuming Uniform deformation model [17]. In crystals, we can observe two types of strain, Uniform strain and non–uniform strain. Uniform strain causes the unit cell to expand or contract in an isotropic way. This simply leads to a change in the unit cell parameters and shift of the peaks. There is no broadening associated with this type of strain. Non–uniform strain leads to systematic shifts of atoms from their ideal positions and to peak broadening. This type of strain arises due to point defects (vacancies, site–disorder), plastic deformation (cold worked metals, thin films) films) and poor crystalline. This model doesn't take into account the anisotropic nature of the crystal. In this model, microstrain **ε** is assumed to be uniform in all crystallographic directions and Hall– Williamson equation can be written as

$$\beta_{hkl}\cos\theta_{hkl} = (K\lambda/t) + (4\langle\varepsilon\rangle \sin\theta_{hkl}).$$

Plotting the measured values of $(\beta_{hkl})_{corrected}$ as a function of $(4\sin\theta_{hkl})$, the microstrain $\langle\varepsilon\rangle$ can be estimated from the slope of the line and the crystallite size from the intersection of the vertical axis. The Hall–Williamson plot assuming uniform deformation model for the sample is shown in Figure 4.

It can be noted that the microstrain and crystallite size contribution can be separated using Hall–Williamson analysis. Further, the microstrain values obtained for the sample is small in magnitude. Strain and particle size are calculated from the slope and y–intercept of the fitted line respectively. From the lattice parameters calculations it was observed that this strain might be due to the lattice shrinkage. The crystallite size obtained when considering the strain contribution using Hall Williamson analysis assuming uniform deformation model is found to be 70 nm. Presence of defects can also affect the anisotropy of the crystal which leads to non–uniform nature of the crystal. For confirmation some other techniques such as Warren–Averbach model and Rietveld analysis have to be employed.

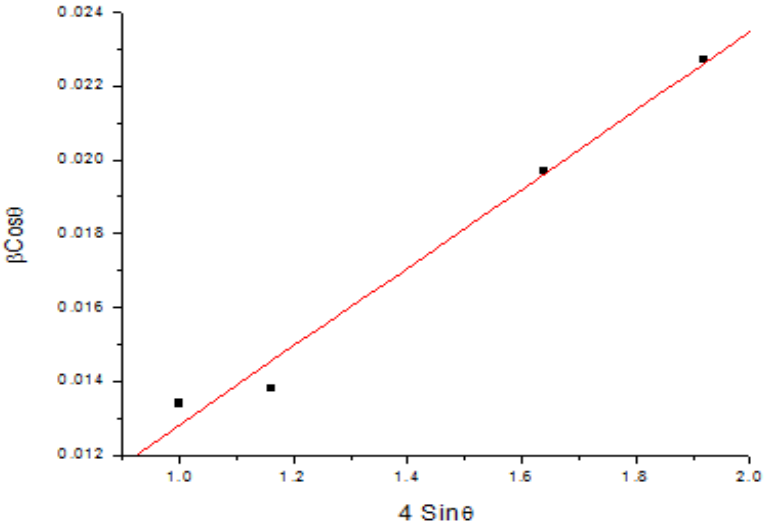

Fig. 4: Hall Williamson Plot of the sample

3.4. Determination of Band gap energy from UV–Visible Absorption Spectra

UV–Visible absorption spectroscopy is widely used for calculating the bang gap energy of semiconductor materials including nanostructured materials. Also UV–Visible spectrum of the samples gives information about excitonic or inter band transition of nanocrystalline materials. From the absorbance value, knowing the concentrations of the samples, absorption coefficient **α** was estimated. The optical band gap of a semiconductor can be estimated using the following equation for semiconductor,

$$\alpha h\nu = A\,(h\nu - E_g)^n$$

where, A is a constant, **α** is the absorption coefficient and E_g isthe band gap of the material. The value of the exponent determines the transition. If the transition is allowed direct n=1/2, for allowed indirect n=2, forbidden direct n=3/2 and forbidden indirect n=3. The exact value of band gap can be determined by plotting $(\alpha h\nu)^{1/n}$ versus hν graph and extrapolating the straight line portion of the graph to hν axis. The UV–Visible spectrum of the sample is shown in Figure 5.

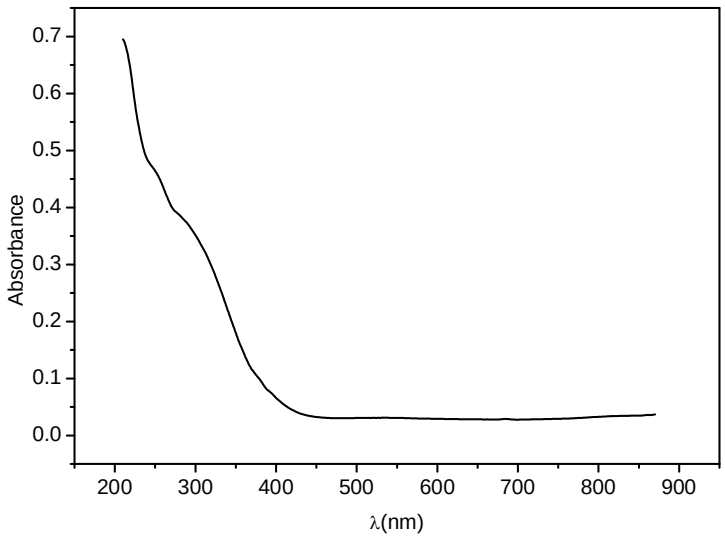

Fig. 5: UV–Visible spectrum of $Pr_2Zr_2O_7$

The optical transition of the sample is reported to be an allowed direct one. Hence in the following analysis the value of n is set as 1/2. Figure 6 shows the plot of $(\alpha h\nu)^2$ versus hν for sample. By extrapolating the straight line portions of the plots, the exact value of the band gap are obtained and was found to be 2.69 eV[18].The Pr compound shows moderate transmittance at UV wavelengths and the blue end ofthe visible range, gradually increasing to a maximum at the red end.The valance band and conduction band of $Pr_2Zr_2O_7$ consist of Pr 4f orbitals and Zr 4d orbitals. The energy gap between these two orbitals strongly depends on the crystallite size. The O 2p orbitals lie below the Pr 4f orbital and do not affect the bandgap of the materials. Hence, the quantum size effect and Pr 4f orbitals affect the bandgap, resulting in the variation of the bandgap energies for these nanoceramics.

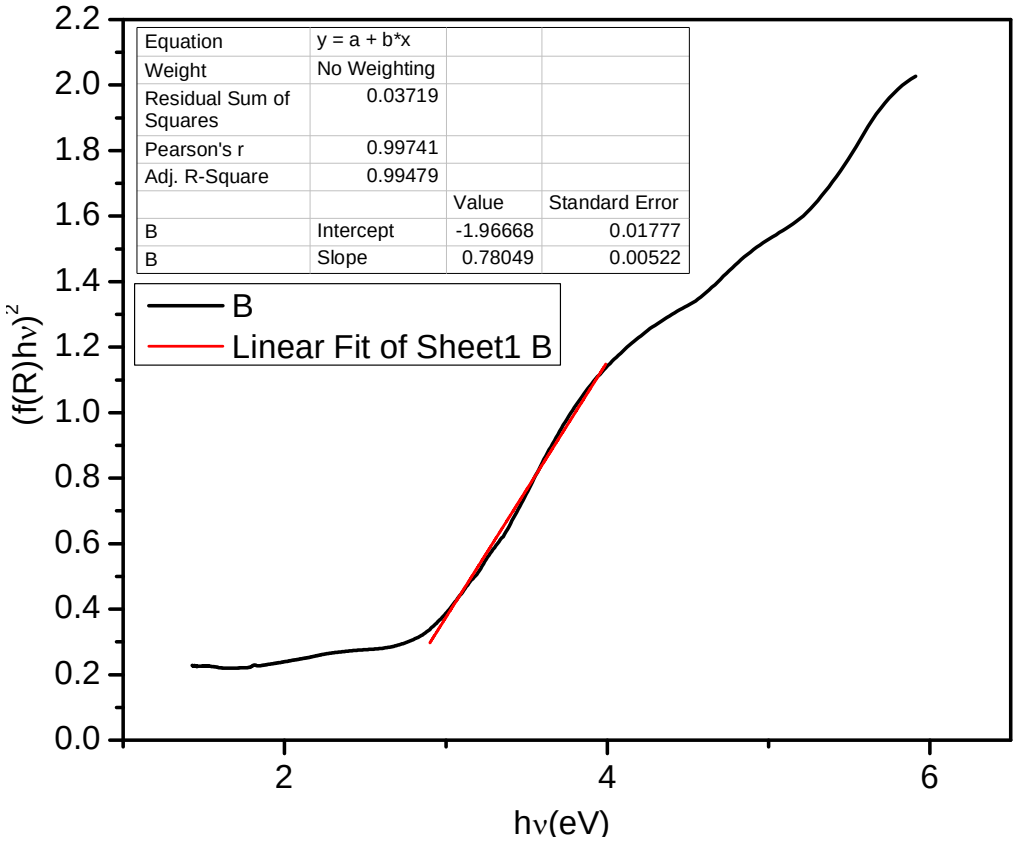

Fig. 6: (f(R)hν)1/n versus hν plot of $Pr_2Zr_2O_7$

4. CONCLUSIONS

A modified combustion process has been developed for the synthesis of nanoparticles of $Pr_2Zr_2O_7$. The xrd analysis concluded that the structure is defect fluorite, having cubic lattice. Average Crystallite size of the sample was calculated from Debey–Scherrer equation is to be 9 nm. Hall Williamson analysis was carried out to separate the strain contribution in X–ray line broadening. The size obtained from the analysis was found to be 70 nm, which is many times higher than as that obtained from Scherrer calculation. This may be due to the anisotropy of the crystal. Band gap energy of the sample was obtained from UV–Visible spectroscopic analysis of the sample. It was found to be 2.69 eV which is in agreement with the wide band gap nature of defect fluorite. This also supports the larger anisotropy of the structure.

REFERENCES

[1] Subramanian M.A., Aravamudan G., SubbaRao G.V., Prog. Solid State Chem., 15, **1983,** 55.
[2] Mandal B.P. and Tyagi A. K., J. Alloys & Comps., 437, **2007,** 260.
[3] Achary S.N., Sali S. K., Kulkarni K., Krishna P.S.R., Shinde A.B., Tyagi A.K., Chem. Mater., 21, **2009,** 5848.
[4] Jan Kuneš, Pickett W. E., Phys B: Cond. Matter, 378, **2006,** 898.
[5] Mandal B. P., Deshpande S. K. and Tyagi A. K., J. Mater. Res., 23, **2008,** 911.
[6] Sickafus K.E., Minervini L., Grimes R.W., Valdez J.A., Ishimaru M., Li F., McClellan K. J., Hartmann T., Science, 289, **2000,** 748.
[7] Patil K. C., Aruna S. T. and Mimani T., Curr. Opin. Solid State Mater. Sci., 7, **2002.**
[8] Jain S. R., Adiga K. C., and Pai Verneker V. R., Combust. Flame, 40, **1981,** 71.
[9] Mimani T. and Patil K. C., Mater. Phys. Mech., 4, **2001,** 134.
[10] Prakash A. S., Khadar A. M. A., Patil K. C. and Hegde M. S., Journal of Materials Synthesis and Processing, 10, **2002,** 135–141.
[11] Prabhu Y. T., Venkateswara Rao K., Sesha Sai Kumar V., Siva Kumari B., International Journal of Engineering and Advanced Technology, 3, **2013,** 268– 275.
[12] Yendrapati Taraka Prabhu, Kalagadda Venkateswara Rao, Vemula Sesha Sai Kumar, Bandla Siva Kumari, World Journal of Nano Science and Engineering, 4, **2014,** 21–28.
[13] Deepa M., Prabhakar Rao P., Radhakrishnan A. N., Sibi K. S. and Koshy P., Mater. Res. Bull., 44, **2009,** 1481–1488.
[14] Sibi K. S., Radhakrishnan A. N., Deepa M., Prabhakar Rao P. and Koshy P., Solid State Ionics, 180, **2009,** 1164–1172.
[15] Radhakrishnan A. N., Prabhakar Rao P., Mary Linsa K. S., Deepa M. and Peter Koshy, Dalton Transations, 40, **2011,** 3839–3848.
[16] Barnita Paul, Kushal Singh, Tomasz Jaroń, Anushree Roy, Anirban Chowdhury, Journal of Alloys and Compounds, 686, **2016**, 130–136.
[17] Mote V.D. , Purushotham Y., Dole B.N., Journal of Theoretical and Applied Physics, 6, **2012**, 1–8.
[18] Sam Solomon, Aneesh George, Jijimon Kumpakkattu Thomas and Annamma John, Journal of Electronic Materials, 44, **2015,** 28–37.